

Detection of Gravitational Waves Using Bayesian Neural Networks

Yu-Chiung Lin and Jiun-Huei Protty Wu*

*Department of Physics, Institute of Astrophysics, and Center for Theoretical Physics,
National Taiwan University, Taipei 10617, Taiwan*

We propose a new model of Bayesian Neural Networks to not only detect the events of compact binary coalescence in the observational data of gravitational waves (GW) but also identify the time periods of the associated GW waveforms before the events. This is achieved by incorporating the Bayesian approach into the CLDNN classifier, which integrates together the Convolutional Neural Network (CNN) and the Long Short-Term Memory Recurrent Neural Network (LSTM). Our model successfully detect all seven BBH events in the LIGO Livingston O2 data, with the periods of their GW waveforms correctly labeled. The ability of a Bayesian approach for uncertainty estimation enables a newly defined ‘awareness’ state for recognizing the possible presence of signals of unknown types, which is otherwise rejected in a non-Bayesian model. Such data chunks labeled with the awareness state can then be further investigated rather than overlooked. Performance tests show that our model recognizes 90% of the events when the optimal signal-to-noise ratio $\rho_{\text{opt}} > 7$ (100% when $\rho_{\text{opt}} > 8.5$) and successfully labels more than 95% of the waveform periods when $\rho_{\text{opt}} > 8$. The latency between the arrival of peak signal and generating an alert with the associated waveform period labeled is only about 20 seconds for an unoptimized code on a moderate GPU-equipped personal computer. This makes our model possible for nearly real-time detection and for forecasting the coalescence events when assisted with deeper training on a larger dataset using the state-of-art HPCs.

I. INTRODUCTION

Since the first detection of gravitational waves (GWs) on September 14th, 2015 [1], the advanced Laser Interferometer Gravitational Wave Observatory (aLIGO) [2], later joined by the advanced Virgo [3] in 2017, has detected ten coalescence events for binary black holes [1, 4–9] and one for binary neutron stars [10] during its O1 and O2 observation runs. The triumph also comes with a remarkable milestone where the electromagnetic counterparts of the binary neutron star coalescence event GW170817 [10] was discovered [11–13]. The success of LIGO and Virgo has opened a new era of multi-messenger astronomy, allowing for independent measurement of Hubble constant [14] and constraints on theoretical models such as cosmic strings [15]. Two new GW detectors located in Japan [16] and India [17] respectively are about to join the network in order to increase the overall sensitivity and the precision in sky locations of the sources. While more detectors join the network, the need for techniques of real-time detection has become more pressing not only for accurate determination of sky source locations but also for the counterpart observations such as those for electromagnetic signals [18]. However, the commonly used match-filtering techniques [19–23] are computationally expensive, making it a great challenge for real-time detection.

Recently the deep learning technique based on artificial neural networks [24] is considered as a promising alternative to the matched-filtering method. Various types of Deep Neural Networks (DNNs) such as the Convolutional Neural Network (CNN) [25] and the Long Short-

Term Memory Recurrent Neural Network (LSTM) [26] have shown great potential in the framework of GW research, especially for real-time detection [27–33], parameter estimation [27, 28, 31], glitch recognition [34–37] and data denoising [38–40]. However, despite their potential prospect, the DNN models usually suffer from overfitting and thus are difficult to be generalized for making reliable predictions in face of new-type data. In addition, most DNN models are deterministic in a way that they offer only one rigid prediction for each given set of input. A deterministic model can hardly provide uncertainty information about its predictions. Therefore the problems of overfitting and lack of uncertainty estimation make the DNN models unreliable, sometimes giving overconfident predictions on out-of-distribution data [41].

In order to deliver the uncertainty information, we need to convert the traditional deterministic model into a probabilistic model. In the field of deep learning, the Bayesian Neural Network (BNN) [42, 43], which updates its weights via Bayes’ rule, is a potential choice for this purpose. The BNN technique is not only capable of providing uncertainty estimation but also resistant to overfitting. In addition, it can be trained with a rather small dataset. The uncertainty estimation is particularly useful in face of the out-of-distribution data and could assist further training for data augmentation. Although the BNN is more computationally expensive than the deterministic DNN, it is totally feasible when assisted with the recent-year advances in both the hardware and the approximation algorithms [44–49].

In this paper we use the Variational Inference (VI) approximation [45–47, 50] to construct a Convolutional, Long Short-Term Memory, Fully-Connected Deep Neural Network (CLDNN) model [51]. The incorporation of the sliding-window search scheme enables us to identify the

* jhpw@phys.ntu.edu.tw

time period of the GW waveform in a coalescence event. This feature distinguishes our model from other CNN models for GW detection in literature. The combination of a Bayesian approach and the CLDNN is also a unique feature of our model. Based on the model prediction and its estimated uncertainty, our Bayesian model can rapidly flag each of the sequential time windows with a trigger state, a noise state, or a state that needs further attention. The estimated uncertainty can also serve as a reference for the significance level of a prediction. Our model is not to replace the matched-filtering search or other models of parameter estimation but to serve as a prior process for efficiently identifying the time windows of signals and those which may contain new-type signals. Our model also enables the possibility for nearly real-time detection, which is unlikely to be feasible for the usually time-consuming matched-filtering search.

We organize this paper as follows. In Section II, we introduce our BNN-based method, including the model architecture, data preparation, training procedure, and the flagging strategy. In Section III, we demonstrate with uncertainty estimation the capability of our model in detecting gravitational waves, first with benchmarking tests and then against the real data from LIGO. In Section IV we discuss several critical issues in our model and its potential for event prediction. Finally we conclude our work in Section V.

II. BAYESIAN NEURAL NETWORKS FOR GRAVITATIONAL WAVE DETECTION

A. Bayesian Neural Network

The Bayesian Neural Network [42, 43] is the Deep Neural Network that uses probability distributions, instead of point values, as weights and biases. The BNN can provide uncertainty estimation about its prediction and handle overfitting. The parameters in a BNN model are initialized with prior distributions $p(W)$, where W represents the model weight. When trained with a given dataset \mathcal{D} , these prior distributions are updated to posterior distributions $p(W|\mathcal{D})$ via the Bayes' Rule:

$$p(W|\mathcal{D}) = \frac{p(\mathcal{D}|W)p(W)}{p(\mathcal{D})}, \quad (1)$$

where $p(\mathcal{D}|W)$ is the likelihood and $p(W)$ is the model evidence. One can then obtain the predictive distribution, $p(\mathbf{y}^*|\mathbf{x}^*, \mathcal{D})$, for a new input \mathbf{x}^* as

$$p(\mathbf{y}^*|\mathbf{x}^*, \mathcal{D}) = \int p(\mathbf{y}^*|\mathbf{x}^*, W)p(W|\mathcal{D})dW. \quad (2)$$

However, for most of the modern neural networks the posterior $p(W|\mathcal{D})$ cannot be analytically calculated or efficiently sampled due to the enormous number of parameters in the model. To tackle this problem we employ the Variational Inference (VI) [45, 52], which approximates

the true posterior $p(W|\mathcal{D})$ with some tractable distributions $q_{\theta}(W)$ that can be fully parametrized by θ . For example, the commonly used Gaussian distribution can be parametrized by the mean μ and standard deviation σ . The training goal is to minimize the negative evidence lower bound (ELBO): [45, 46]

$$\mathcal{F}(\theta) = -\mathbb{E}_{W \sim q_{\theta}} [\log p(\mathcal{D}|W)] + \text{D}_{\text{KL}}(q_{\theta}||p), \quad (3)$$

where the first term is the expectation value of negative log likelihood and the second term is the Kullback-Leibler divergence [53, 54] between distributions q_{θ} and p . In classification tasks, the first term is equivalent to the cross-entropy loss.

Within the framework of currently available machine learning tools, the VI estimator used in BNNs is usually achieved by perturbing the weights and biases [45–48]. At each forward pass, the model weights and biases are randomly sampled from the distributions $q_{\theta}(W)$. If the distributions are independent Gaussian distributions, the gradients can be computed using back propagation [48]. Thus the predictive distributions can be approximated by propagating the input \mathbf{x}^* through the model multiple times and then taking the average:

$$\begin{aligned} p(\mathbf{y}^*|\mathbf{x}^*, \mathcal{D}) &\approx \int_W p(\mathbf{y}^*|\mathbf{x}^*, W)q_{\theta}(W)dW \\ &\approx \frac{1}{N} \sum_{i=1}^N p(\mathbf{y}^*|\mathbf{x}^*, W_i), W_i \underset{i.i.d.}{\sim} q_{\theta}(W), \end{aligned} \quad (4)$$

where N is the number of Monte-Carlo samples. However, for a mini-batch training the samples in a batch usually share the same weight perturbation for computational efficiency, and this will induce correlation between the gradients and thus make the model hard to converge due to the high variance in the gradient estimation [47]. In addition, it is hard to conduct inference for unknown samples of shared weight perturbations because we are forced to propagate one sample through the model at a time in renewing the weight perturbation. To cope with this, Ref.[47] proposed a flipout estimator that applies a random sign matrix on the weight perturbation matrix for each sample, so as to achieve a pseudo-independent weight sampling for each sample in a mini batch. The flipout estimator does not limit the variance reduction effect during training when trained with a large batch, and it also enables the Monte-Carlo (MC) sampling with mini-batch prediction and thus speeds up the prediction process. In this work we use the Bayes by Backprop (BBB) VI method proposed in Ref.[46] in combination with this flipout estimator [47] to train our model.

Uncertainty estimation is an important feature of the BNN, making it more robust for unknown input than the deterministic neural networks. For a softmax classifier, the predictive uncertainty can be defined as the covariance of the predictive distribution [55, 56]:

$$\mathbf{U} = \frac{1}{N} \sum_{i=1}^N (\text{diag}(\mathbf{p}_i) - \mathbf{p}_i^{\otimes 2}) + \frac{1}{N} \sum_{i=1}^N (\mathbf{p}_i - \bar{\mathbf{p}})^{\otimes 2}, \quad (5)$$

where \mathbf{p}_i is the predictive vector of the i -th MC sample, $\bar{\mathbf{p}}$ is the mean predictive vector, and for a given vector \mathbf{v} we define the notations $\mathbf{v}^{\otimes 2} = \mathbf{v}\mathbf{v}^T$ and $\text{diag}(\mathbf{v})$ being a diagonal matrix with elements from \mathbf{v} . The first term in Equation (5) is called the aleatoric uncertainty, which captures inherent randomness of the prediction \mathbf{p}_i . The second term is called the epistemic uncertainty, which originates from the variability of W given the dataset \mathcal{D} . In binary classification the off-diagonal elements in \mathbf{U} normally provide no useful information so we focus only on the diagonal elements, which are the variances of the predictions in each class. Therefore the uncertainty of a prediction on the k -th class can be simplified as [57]:

$$u_k = \frac{1}{N} \sum_{i=1}^N (p_{k,i} - p_{k,i}^2) + \frac{1}{N} \sum_{i=1}^N (p_{k,i} - \bar{p}_k)^2. \quad (6)$$

Because empirically we have $u_k < 0.25$, we intuitively define a confidence score for the k -th class as [57]:

$$c_k = 1 - 2\sqrt{u_k}, \quad (7)$$

which indicates how confident the model is in its prediction.

B. Architecture of our Model

It would be extremely useful if a neural network model for GW detection could also provide information about the duration of a coalescence event, which normally lies between less than a second and tens of seconds depending on the component masses. With the duration information, we would be able to dramatically reduce the search space for component masses and thus speed up the match filtering process. Recent work in Ref. [58] and Ref. [29] proposed fully convolutional neural networks based on the structure of WaveNet [59] that accepts input data of various lengths but their model only triggers the alarm around the GW signal peak while providing no information about the signal duration. Here we propose a model that could provide the duration information.

Our approach is a Convolutional, Long Short-Term Memory, Fully-Connected Neural Network (CLDNN) model [51], which integrates the fixed-length CNN and the sliding-window search. The characteristic of the LSTM that it remembers the state in the previous time step can help us to detect not only the peak signal, which indicates the coalescence event, but also the earlier signals from the inspiral stage. We also address the point noted in Ref. [29]—if one uses the half-length of the CNN window as the stride for a sliding-window approach, although the GW signal may lie only partially within this window the main part of the waveform will be captured by the next window(s) and the LSTM structure can correlate these windows to make meaningful predictions.

As a first step to deliver the above, we choose the input format of our model to be the strain data sliced into

time windows (time steps) of fixed length, each of which is halfly overlapped with its neighbors. The details of data generation will be described in Section II C. There is essentially no limit on the number of windows so our model is suitable for data of any length. Nevertheless in each operation the size of windows needs to be fixed due to the structural requirement of the LSTM and the fully-connected layers.

Our model is composed of three main sequential sectors: the CNN, LSTM, and FC. Fig. 1 shows the structure. The CNN sector has four convolutional blocks, each with four layers: Bayesian convolution, max pooling [60], batch normalization [61], and Rectified Linear Unit (ReLU) activation [62]. The four Bayesian convolution layers have 8, 16, 32, 64 filters with kernel sizes of 16, 8, 8, 8 and strides of 1, 2, 2, 2, respectively. After the convolution the data are flattened and then passed into the LSTM sector.

The LSTM sector has two bidirectional Bayesian LSTM layers, each with 128 hidden units in each direction. Finally the FC sector has two Bayesian Fully-Connected (FC) layers, each with 32 and 2 hidden units respectively. The first Bayesian FC layer is followed by an ReLU activation layer, and the second by a softmax activation layer in order to confine the output values between 0 and 1. All Bayesian layers employ the VI [45, 46, 50] and the flipout technique [47] to generate pseudo-independent weight and bias perturbations in the hidden layers.

Our model has a total of around 4.65 million parameters. Its outputs are the class results (class 0 for noise and class 1 for signal), each attached with a confidence score between 0 and 1 as a reference to judge on the existence of the GW signals from coalescence events in the corresponding time windows.

C. Data Preparation

1. Real Noise Data

In this work we use the LIGO Livingston O2 data segments provided by the Gravitational Wave Open Science Center [63] (GWOSC) as our background noise of GW injection. We select 15 data segment files from the early stage of the observation for training, 5 files from the final stage for validation, and 8 files from the middle for testing the model. All data segment files are 4096 seconds in length and have a quality of at least $\text{CBC_CAT3} = 100$. They do not contain any of the events or marginal triggers published by LIGO [9]. We down sample the sample rate of the strain data from 16384 to 8192 Hz in order to save memory.

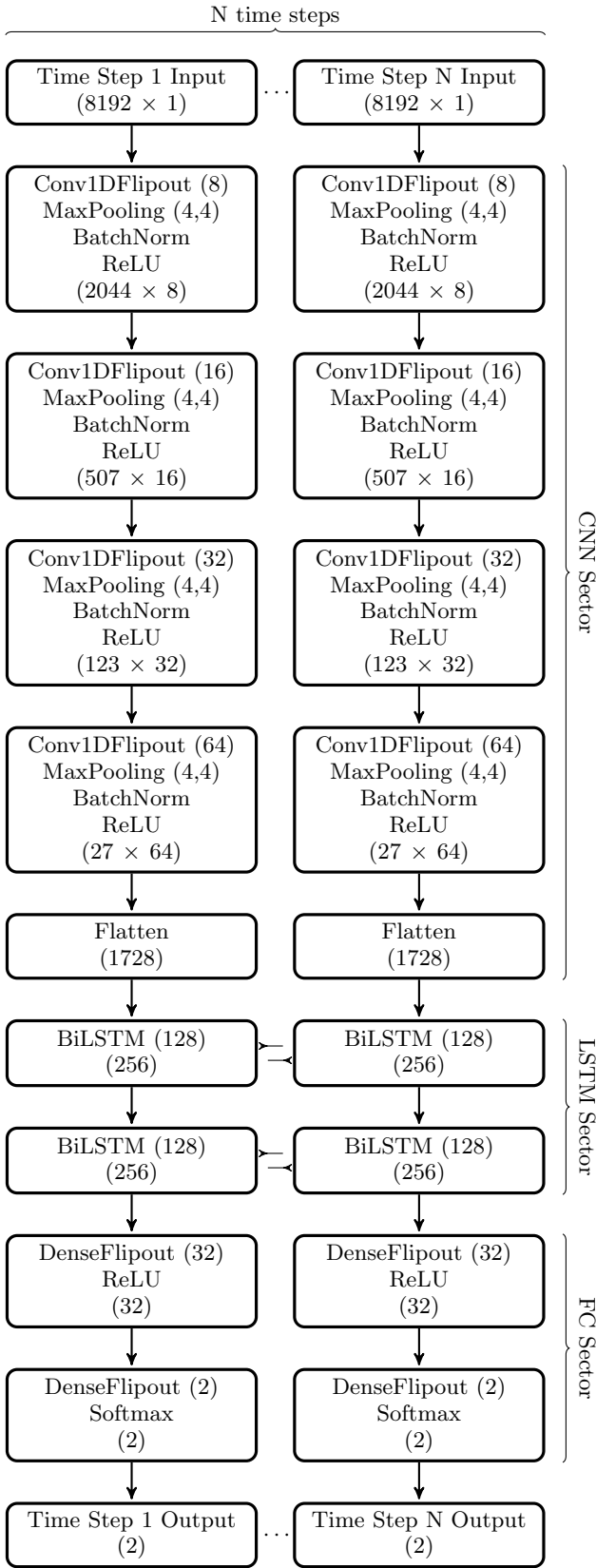


FIG. 1. The structure of our Bayesian CLDNN model. The dimensions of the outputs from each block are indicated at the bottom of each block.

We use the software packages PyCBC [20, 21] and LALSuite [64] to generate GW signals of quasi-circular, non-spinning BBH coalescence with the effective-one-body model SEOBNRv4T [65]. The signals are simulated with a sample rate of 8192 Hz and a cut-off frequency of 20 Hz. The choice of component masses is similar to those in Ref. [27, 28]. For the training dataset the BBH component masses range between $5M_{\odot}$ and $75M_{\odot}$ in steps of $1M_{\odot}$, with a mass ratio of $q = M_1/M_2 \leq 10$. For the validation dataset the masses are offset by $0.5 M_{\odot}$ with respect to those in the training dataset. For the testing dataset the masses are the collection of those values used in the above two datasets. In order to make our simulated samples more realistic, we also incorporate the GPS time stamps (of the associated real noise; see below) and a set of randomly generated right ascension and declination into our dataset following the convention of LIGO L1 detector.

3. Data Generation

In generating the training dataset, we inject the simulated signals (Sec. II C 2) into the real noise randomly picked up from the LIGO dataset (Sec. II C 1). To manipulate the signal-to-noise ratio (SNR), we pre-calculate the power spectral density (PSD) of the noise $S_n(f)$ and tune the strength of the GW signal h so that the optimal SNR, ρ_{opt} , defined by [66]

$$\rho_{\text{opt}}^2 = 4 \int_0^{\infty} df \frac{|\tilde{h}(f)|^2}{S_n(f)}, \quad (8)$$

lies between 5 and 15 with steps of 0.5. Here $\tilde{h}(f)$ is the Fourier transform of h . We then whiten the data using the recalculate PSD. The length of the data in this process is 16 seconds and we keep only the central 8 seconds to avoid FFT artifacts. We also purposely arrange for the signals to peak within the last 2 seconds of this final 8 seconds, in a hope that our model could detect the coalescence event as soon as it comes into the analyzed data. The 2-second diversity in the signal position is expected to lead to a better sensitivity of our model in event position.

We then slice and standardize the whitened data into 15 time windows of 1 second, each with 0.5-second overlaps with its neighbors. Finally, we mark a time window with 1 if it contains a GW signal of longer than 0.25 seconds, or longer than half of the signal duration when the duration is shorter than 0.5 second. All other windows are marked with 0. An example of the simulated data sample is shown in Fig. 2.

To carry out this work, we generate 40960 and 4096 samples for the training dataset and the validation dataset respectively. For the testing dataset we generate

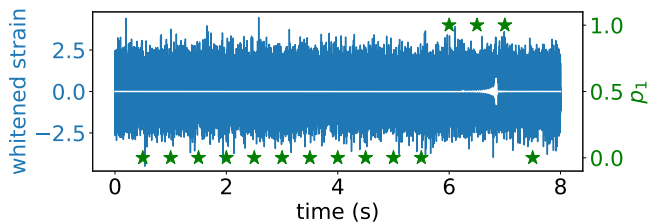


FIG. 2. Simulated LIGO L1 strain data (blue curve) that contain a GW signal (white curve) with $m_1 = 45.0$, $m_2 = 38.5$, $\rho_{\text{opt}} = 8$, right ascension $\pi/4$ and declination $\pi/4$. The green stars are the marks (0 or 1) of the time windows centered at each window.

512 samples for each of the SNRs in the range between 2 and 18 with steps of 0.5. To train our model, we also need null samples so half of the samples in each dataset contain only noise (without GW signals).

D. Training Procedure

To deliver our model, we employ the tools provided by the software packages TensorFlow [67] and the TensorFlow Probability [68]. For the Bayesian LSTM layers we build a customized Bayesian LSTM cell that applies the weight perturbation and the flipout estimator on the hidden kernel, recurrent kernel and bias. The LSTM cell is then wrapped by the ordinary RNN layer functionality provided in TensorFlow. For updating the model weights during training, we use the ADAM [69] optimizer with a scheduled learning rate of

$$\text{lr}(e) = \begin{cases} 0.005, & \text{if } e \leq 15; \\ 0.005 * \exp(0.05 * (15 - e)), & \text{otherwise;} \end{cases} \quad (9)$$

where e is the number of training epoch. We use a combination of the sparse categorical cross entropy and the KL divergence as our loss function. Because in our training scheme the KL divergences of each layer and cell are accumulated into the regularization loss whenever passing through the data, we have to weigh the KL divergence in each layer and cell with the value of $\frac{1}{CN}$ [50], where C is the number of time steps in a sample and N is the total number of samples for training, so that it is applied only once per epoch. Otherwise the accumulated large KL divergence will over-regularize the model and eventually stop the model from learning.

About the hardware, we train our model of 150 epochs and a batch size of 256 on a computer with Intel[®] Core[™] i5 6500 CPU and AMD[™] RX 480 GPU. Even with such moderate computational power and a code of Bayesian LSTM cell unoptimized for GPU, the whole training process normally takes only about 50 hours. This is a critical feature of our work. After the last epoch we save only the model parameters because we want to minimize the KL loss, which keeps decreasing during the training.

E. Flagging Strategy

Our model performs tasks of binary classification, with a predictive value of p_1 indicating the identification for GW signals and a value of p_0 for noise, where $p_0 + p_1 = 1$. Thus we need to keep only p_1 for subsequent analysis. We also calculate the average predictive value \bar{p}_1 and the confidence score c_1 for \bar{p}_1 using Equations (4) and (7) respectively.

Considering the issue of confidence level in statistics, we weigh the \bar{p}_1 with its confidence score c_1 . This is to avoid our model from accepting or rejecting a time window for signals when the confidence score c_1 is low. Thus we flag all the time windows with three distinct states: *trigger*, *noise* and *awareness*. A time window t is flagged with a trigger state when the trigger score defined as

$$s_t = \bar{p}_{1,t} \times c_{1,t}, \quad (10)$$

is larger than 0.5, where $\bar{p}_{1,t}$ and $c_{1,t}$ are the \bar{p}_1 and c_1 of the time window t respectively. Such s_t can be regarded as the significance level of a detection.

Similarly a time window t is flagged with a noise state when the noise score defined as

$$\begin{aligned} n_t &= \bar{p}_{0,t} \times c_{0,t}, \\ &= (1 - \bar{p}_{1,t}) \times c_{1,t}, \end{aligned} \quad (11)$$

is larger than 0.5. We note that in a system of binary classification, $c_{0,t}$ equals $c_{1,t}$. We also note that $s_t + n_t = c_{1,t}$.

Those time windows that are not flagged with a trigger state nor a noise state will be flagged with an awareness state. The role of such a state can be illustrated in a Bayesian dog-null classifier for images when we feed it with an image of cat. It is likely that the classifier will give a reasonable p_1 but low c_1 . In such a case we can only say that the model ‘notices’ something though not sure what it is.

As a demonstration we apply the above flagging strategy to the data presented in Fig. 2 and the results are shown in Fig. 3. Because the flipout estimator enables batch prediction, we use a batch size of 32 to dramatically accelerate the MC sampling process (see Sec. IV A). As shown in Fig. 3, among the three time windows that are marked with 1 (green stars) for indicating the GW singles, our model flag two with trigger states (cyan stars) and one with an awareness state (cyan triangle) likely due to the much weaker signal within this time window. This demonstrates the usefulness of the awareness state in practice, which has actually incorporated the sliding-window search. In Fig. 3 we also show the confidence score $c_{1,t}$ (orange dots), the averaged predictive probability for being a signal $\bar{p}_{1,t}$ (red dots), the distribution of $p_{1,t}$ (pink areas), and the 90% intervals of $p_{1,t}$ (red error bars), all obtained from a set of data sampled for 4096 times.

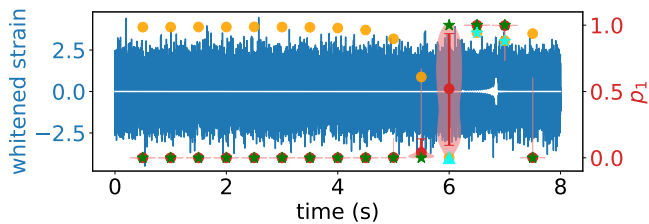


FIG. 3. The prediction with flagging results from our model for the input data presented in Fig. 2. The cyan markers indicate the trigger scores s_t (Eq. (10)), where two trigger states are shown as stars and one awareness state as a triangle. We also show the confidence score $c_{1,t}$ (orange dots), averaged probability for being a signal $\bar{p}_{1,t}$ (red dots), distribution of $p_{1,t}$ (pink areas), and the 90% intervals of $p_{1,t}$ (red error bars), all obtained from a set of data sampled for 4096 times.

It is obvious that the awareness state is associated with a low confidence score $c_{1,t}$, which indicates a large uncertainty in a prediction. It suggests the need for further investigations on this particular time window. In practice, we could ignore these awareness states if we have had trigger states next to them because the purpose of our model is to detect signal events. However if the awareness states do not come with any neighboring trigger states, we could pursue further investigations in order not to miss any detection opportunities for signals of even unknown types. In a training process, on the other hand, these awareness states together with their known markers can be further incorporated into a retraining process, so that the retrained model could become more capable in discriminating between the signals and the noise rather than putting either into the awareness state.

III. RESULTS

A. Performance against Mock Data

To quantify the performance of our model, we take four different measures, namely the TPR, TER, FPR, and FER as defined below, against the dataset generated in Section II C. The sample size in obtaining \bar{p}_1 and c_1 is 4096. Because our model classifier gives three states instead of two, we cannot apply the commonly used confusion matrix to obtain the sensitivity or the false positive rate for our results.

The first measure is the ‘true positive rate’ (TPR), which is the ratio of the trigger states plus the awareness states among all the time windows marked with ‘1’ (with GW signals). To be precise, among all the time windows marked with 1, if the numbers of states for trigger, awareness, and noise are N_{trg} , N_{aw} , and N_{noi} respectively, then the TPR is defined as

$$\text{TPR} = \frac{N_{\text{trg}} + N_{\text{aw}}}{N_{\text{trg}} + N_{\text{aw}} + N_{\text{noi}}}. \quad (12)$$

Such TPR can be regarded as the ‘waveform sensitivity’, which indicates how well the model can capture the waveform structure. Fig. 4 shows the results. It is clear that for GW signals with an SNR of $\rho_{\text{opt}} > 8$, our model detects or is aware of more than 90% of the time windows in the GW waveforms. The persistent awareness rate of about 20% at high ρ_{opt} is due to the obscuration from the noise at the beginning parts of the waveforms, which are always weaker than the noise. In principle this rate of 20% could be reduced if we retrain the model with these marked awareness states.

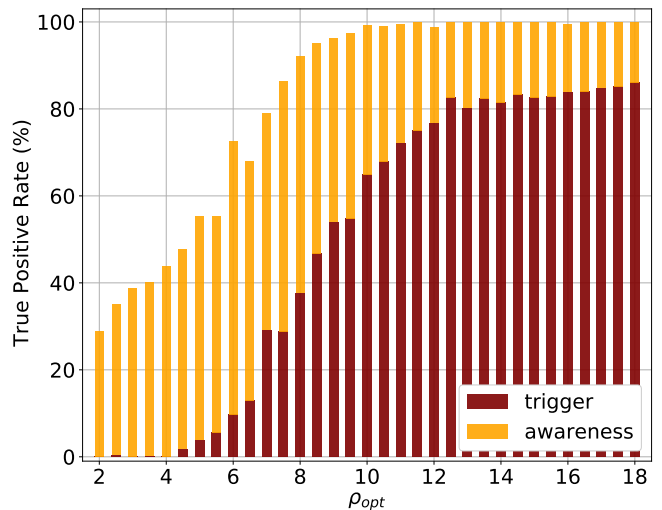


FIG. 4. The True Positive Rate (TPR) as a function of the SNR ρ_{opt} in the performance test of our model. The TPR reaches 90% when $\rho_{\text{opt}} > 8$.

The second measure is the ‘true event rate’ (TER), which is the ratio of the events with at least one trigger or awareness among all the events with GW signals. Among all the signal events, if the numbers of events with ‘at least one trigger’, with ‘awareness only’, and with ‘noise only’ are E_{trg} , E_{aw} , and E_{noi} respectively, then the TER is defined as

$$\text{TER} = \frac{E_{\text{trg}} + E_{\text{aw}}}{E_{\text{trg}} + E_{\text{aw}} + E_{\text{noi}}}. \quad (13)$$

Such TER can be regarded as the ‘event sensitivity’, which indicates how well our model can pick up the true events. Fig. 5 shows the results. Our model achieves a TER of 90% when $\rho_{\text{opt}} > 7$ and 100% when $\rho_{\text{opt}} > 8.5$. For $\rho_{\text{opt}} > 11$ we still see few cases with awareness only and our investigation shows that this is due to some outliers in the noise leading to low confidence.

In comparing the TPR and TER results, it is quite encouraging to see the capability of our model in detecting the GW events (TER), and in shaping the waveforms (TPR) though with a slightly lower sensitivity.

On the other hand, we could define two similar measures for false detections. Thus the third measure is the ‘false positive rate’ (FPR), which is the ratio of the trigger states plus the awareness states among all the time

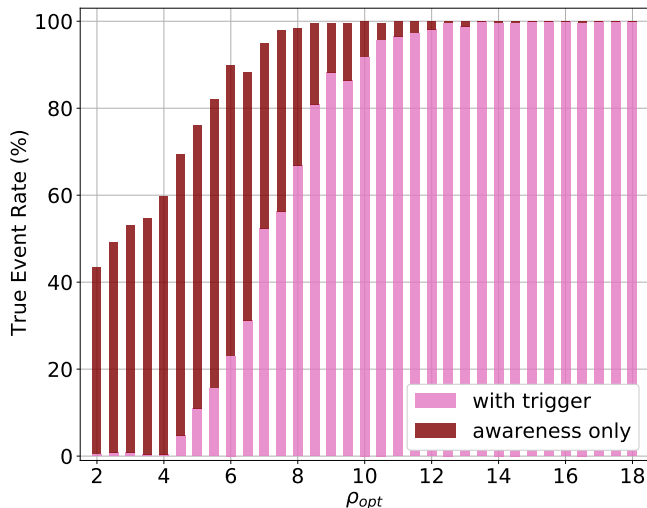


FIG. 5. The True Event Rate (TER) as a function of the SNR ρ_{opt} in the performance test of our model. The TER reaches 90% when $\rho_{\text{opt}} > 7$.

windows marked with ‘0’ (without GW signals). In other words, among all the time windows marked with 0, if the numbers of states for trigger, awareness, and noise are N_{trg}^0 , N_{aw}^0 , and N_{noi}^0 respectively, then the FPR is defined as

$$\text{FPR} = \frac{N_{\text{trg}}^0 + N_{\text{aw}}^0}{N_{\text{trg}}^0 + N_{\text{aw}}^0 + N_{\text{noi}}^0}, \quad (14)$$

which is the sum of the ‘false trigger rate’ $N_{\text{trg}}^0/(N_{\text{trg}}^0 + N_{\text{aw}}^0 + N_{\text{noi}}^0)$ and the ‘false awareness rate’ $N_{\text{aw}}^0/(N_{\text{trg}}^0 + N_{\text{aw}}^0 + N_{\text{noi}}^0)$. This FPR indicates how likely our model will falsely capture the waveform signals. Because the false detections are measured in a background of pure noise, the FPR is not a function of the SNR. Our model shows a false trigger rate of 0.067% and a false awareness rate of 19.6%, summed up to an FPR of about 19.7%. The false trigger rate is unnoticeably small and they are mainly due to the glitches in the noise. We should be able to further reject such triggers when performing the coincidence test. On the other hand we notice that the false awareness rate decreases with the size of the noise dataset for training, so the current unignorable 19.7% is simply due to the smallness of our noise training dataset, which contains limited variability in the background noise.

The last measure is the ‘false event rate’ (FER), which is the ratio of the events with at least one trigger or awareness among all the null events without GW signals. Among all the null events, if the numbers of events with ‘at least one trigger’, with ‘awareness only’, and with ‘noise only’ are E_{trg}^0 , E_{aw}^0 , and E_{noi}^0 respectively, then the FER is defined as

$$\text{FER} = \frac{E_{\text{trg}}^0 + E_{\text{aw}}^0}{E_{\text{trg}}^0 + E_{\text{aw}}^0 + E_{\text{noi}}^0}, \quad (15)$$

which is the sum of the ‘false event trigger rate’ $E_{\text{trg}}^0/(E_{\text{trg}}^0 + E_{\text{aw}}^0 + E_{\text{noi}}^0)$ and the ‘false event awareness rate’ $E_{\text{aw}}^0/(E_{\text{trg}}^0 + E_{\text{aw}}^0 + E_{\text{noi}}^0)$. Our model shows a false event trigger rate of 0.485% and a false event awareness rate of 47.2%, summed up to an FER of about 47.7%. This shows that while our model is capable of detecting the true events as previously seen, it falsely over-predicts the signal events. Again this is simply due to the smallness of our noise dataset for training and can be improved by enlarging the noise training dataset as well as going deeper in the training.

B. Performance against Real Data

In this section we test our model with the LIGO Livingston O2 data that contain confidence detections of BBH coalescence events [6–9, 70].

We downloaded the 32-second strain data from GWOSC, down sampled them to 8192 Hz, calculated the PSD, whitened the data, and then took the 8-second chunks that contain the events in their last seconds. As in the training process, each chunk of the real data here was also sliced into 15 one-second windows with a stride of 0.5 second. For each chunk of the event data, we performed an MC sampling of size 4096, with a batch size of 32. When operated on a moderate GPU-equipped PC, the whole process of flagging took only about 20 seconds for each chunk. Thus our model should be able to achieve nearly real-time detection if we employ better hardware and optimize the Bayesian LSTM layer in gaining the full GPU support. Shorter data chunks and a smaller size of the MC sampling should also help on this.

The results for the BBH coalescence events are shown in Fig. 6. The symbols and colors in these plots follow the same definitions as in Fig. 2 and Fig. 3. For reference purpose, we also plot the whitened GW waveforms (white curves) reconstructed from the values of component masses, luminosity distances, right ascensions and declinations provided in Ref. [9] using the SEOBNRv4T model. The whitened strain data were bandpassed between 30 Hz and 2 kHz.

It is clear that our model successfully detected all the events. It is also important to note that our model successfully triggered all the time windows that contained the GW170608 signal, which spanned a period of nearly 7 seconds. This demonstrates the capability of our model in capturing the full length of a long-duration GW signal. While in literature the matched-filtering search detected GW170729 with rather high false alarm rate [9, 70], our detection of GW170729 also comes with a relatively lower confidence score. This is likely due to the noise fluctuation in the background and could be improved by deepening the model or increasing the size of the training dataset.

Although our model was trained with only the BBH coalescence events, we experimentally tested our model against a binary-neutron-star (BNS) coalescence event,

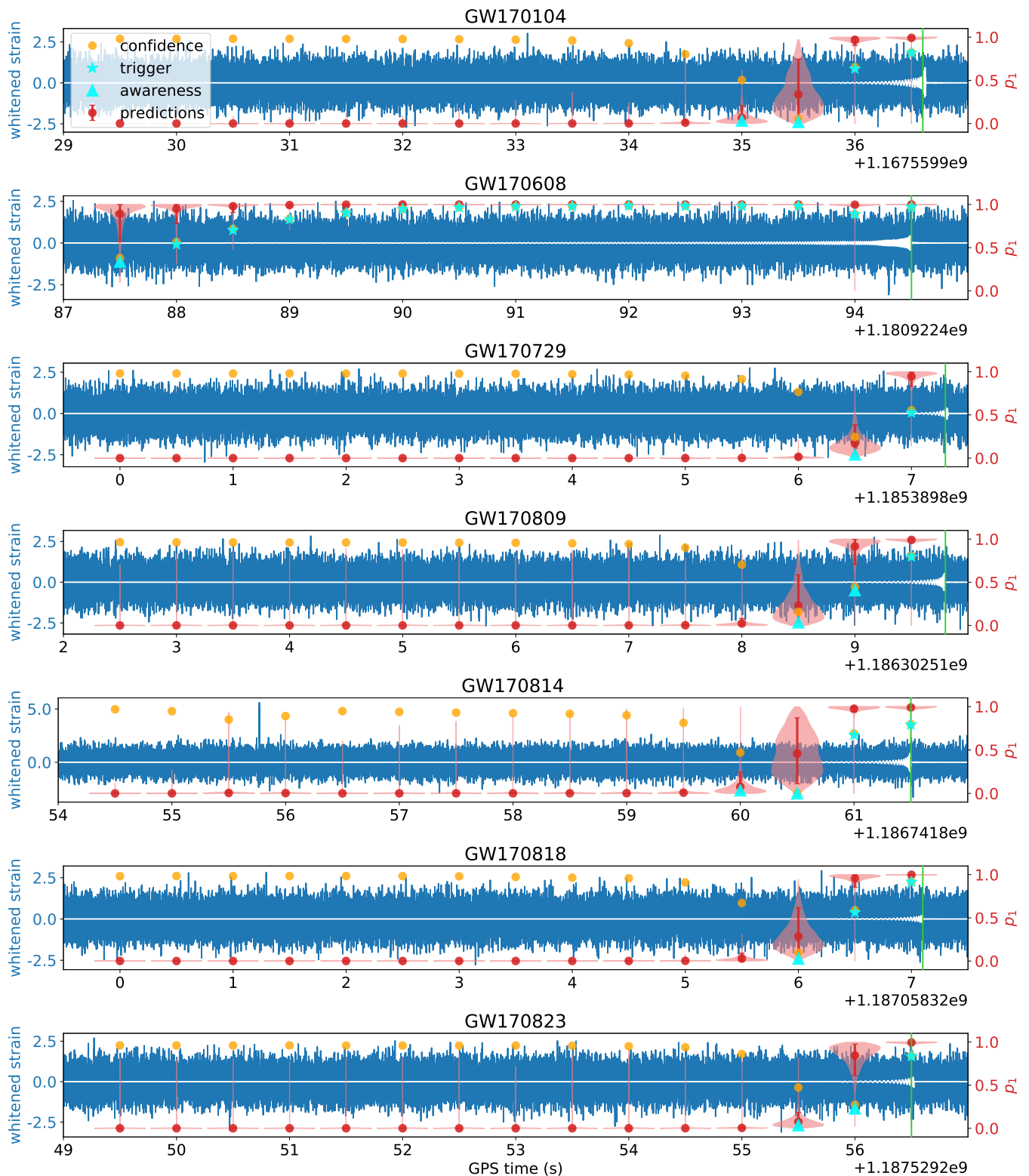


FIG. 6. Successful flagging results of our model for the LIGO Livingston O2 data that contain GW signals from BBH coalescence events. The green vertical lines indicate the event times. Other symbols and colors in these plots follow the same definitions as in Fig. 2 and Fig. 3.

the GW170817 [10], which has masses of $1.27 M_{\odot}$ and $1.46 M_{\odot}$. Fig. 7 shows the result. For this particular

set of Livingston O2 data where there was a large glitch about 1.1 seconds before the event [10], we employed a

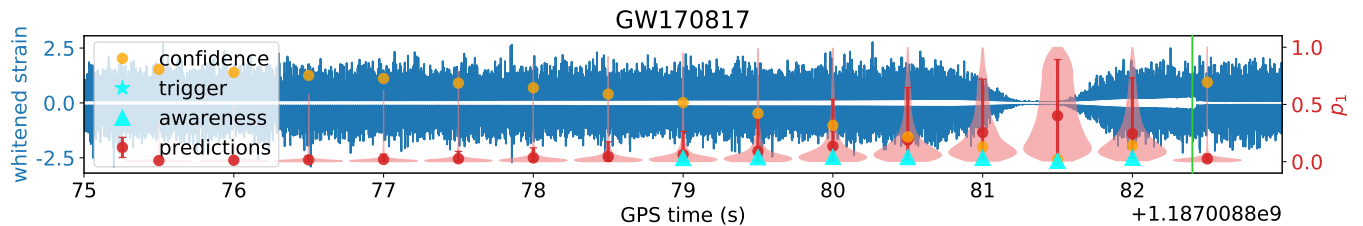


FIG. 7. The flagging results of the LIGO Livingston O2 data set GW170817, which contains a BNS coalescence event. Here we have applied an inverse Tukey window [10, 71] to mitigate the glitch that occurred about 1.1 second before the event.

method used for the rapid reanalysis in Ref. [10, 71] to mitigate this large glitch. The method applies an inverse Tukey window to zero out the data around the glitch. For reference purpose we also plotted the reconstructed GW waveform (white curve) using the TaylorT4 model [72]. As shown in Fig. 7, our model was only aware (with no triggers) of the time windows that contained the BNS waveform and event.

To quantify how much our result had been affected by the Tukey window, which actually deformed the strain data and can be thought as an adversarial example [73, 74], we performed the following three runs for cross validation (see Fig. 8). With the same normal noise background (without glitches) from the LIGO Livingston O2 data, the first run contained a BNS waveform same as shown in Fig. 7 to mimic the GW170817, without any window treatment (top panel in Fig. 8); the second run contained no waveform but applied with an inverse Tukey window (middle panel in Fig. 8); the third contained a BBH waveform to mimic a loud BBH event ($m_1 = 8.5 M_\odot$, $m_2 = 6.0 M_\odot$, and $\rho_{\text{opt}} = 12$), with an inverse Tukey window (bottom panel in Fig. 8). It is evident that our model falsely rejected the GW170817-like signal in the top panel and falsely raised awareness for the Tukey window in the middle panel, but correctly raised triggers for the BBH event in the bottom panel without being affected by the Tukey window. We also note that the $\bar{\rho}_1$ in the middle panel exhibits a behavior similar to the one shown in Fig. 7. Therefore it is likely that the awareness seen in the GW170817 (Fig. 7) is due to the treatment involving the Tukey window.

We further investigated the sensitivity of our model for the BNS events. Fig. 9 shows an example where the BNS signal is as loud as $\rho_{\text{opt}} = 40$, considered as a nearby event closer to the observer. In this case our model was aware of most time windows containing the waveform but still falsely gave low $\bar{\rho}_1$ with significant confidence scores near the coalescence event. This means that our model that was trained with the BBH events (of total component mass larger than $10 M_\odot$) is insensitive to the BNS events. This is not too surprising because the BNS events involve a much smaller mass range and thus could have quite different features in their GW waveforms as compared with the BBH events. To possess sensitivity for the BNS events, we would need to add the BNS waveform

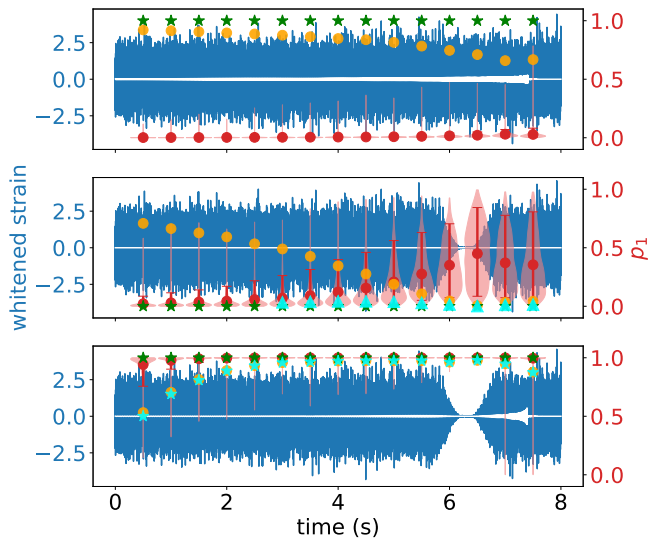


FIG. 8. Three runs for cross validation to test the influence of a Tukey window on the GW170817 result in Fig. 7. With the same normal noise background from the LIGO data, the first run contained a BNS waveform same as shown in Fig. 7 to mimic the GW170817, without any window treatment (top panel); the second run contained no waveform but applied with an inverse Tukey window (middle panel); the third contained a BBH waveform to mimic a loud BBH event, with an inverse Tukey window (bottom panel).

templates into our training dataset.

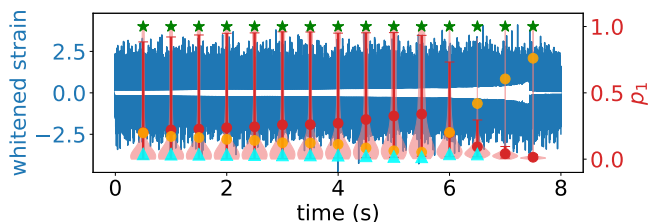


FIG. 9. The flagging result of a loud BNS event with $\rho_{\text{opt}} = 40$.

From the above results especially from the tests for cross validation, we learn that a treatment involving the Tukey windowing will not affect our model for detecting

the BBH events but will affect the cases where no BBH events are present, no matter the data contain a BNS event or not. To be more precise, our current model, trained with only the BBH events, is much more sensitive to the BBH events than the Tukey windowing or the BNS events.

IV. DISCUSSION

In this section we discuss various critical issues in our model, further demonstrating its strengths and future potentials.

A. Size of Monte-Carlo Sampling

The first is about the trade-off between efficiency and accuracy in our Bayesian Neural Networks. In theory the accuracy of BNN increases monotonically with the size of Monte-Carlo sampling, which is the main determinant of the required computation time. Thus there is no natural way for achieving both high accuracy and high efficiency. For example a smaller sampling size helps speed up the prediction process while on the other hand inducing larger uncertainty in the predicted \bar{p}_1 and c_1 . To find a proper trade-off we quantified the dependence of both the prediction uncertainty and the computation time separately on the MC sampling size and also on the batch size for the flipout estimator, which enables parallel predictions (see Sec. II).

About MC sampling, we considered the sizes of 128, 256, 512, 1024, 2048, 4096, 8192, and 16384, each conducted for 100 times with the data in Fig. 2 to obtain the averaged variances in \bar{p}_1 and c_1 and the average computation time. The batch size for the flipout estimator is 32 throughout this test. The left panels in Fig. 10 show the results. As expected, while both the variances in \bar{p}_1 and c_1 decrease with the sampling size, the computation time increases linearly. Based on these results, we chose 4096 as a reasonable trade-off size for the MC sampling.

About the batch size for the flipout estimator, we considered the sizes of 2, 4, 8, 16, 32, 64, 128, 256, and 512, all with the same total sampling size of 4096 and conducted for 100 times using the data in Fig. 2. This test is to understand whether or not a larger batch size does improve much on the computation time, because a larger batch size actually comes with a possible price of sampling bias. The right panels in Fig. 10 show the results. It is clear that the gain in computation efficiency follows the expected behavior of linearity but only for batch sizes up to about 32 but then becomes marginal for larger batch sizes.

For the above reasons, we chose to perform all the predictions in this work (as in Sec. III) with the sampling size of 4096 and the batch size of 32. In principle, one should increase the sampling size while keeping the batch size small whenever practically feasible.

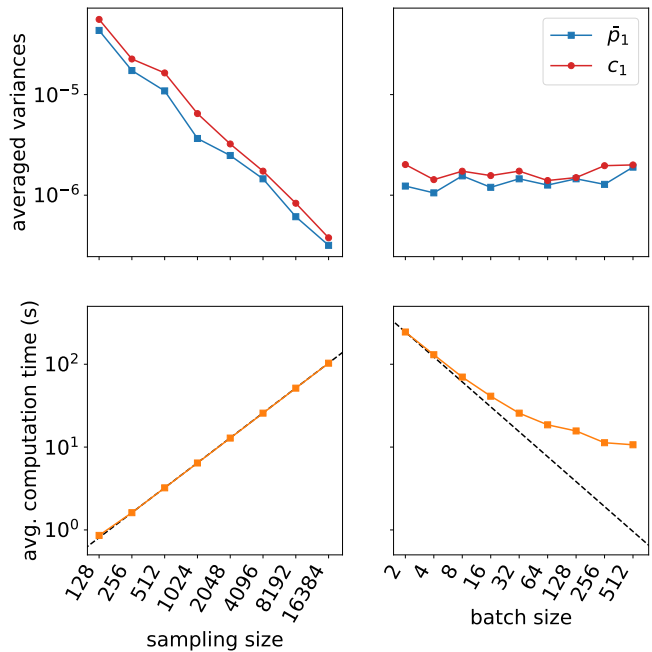


FIG. 10. The left panels show the dependence of averaged variances in \bar{p}_1 and c_1 (top) and of the average computation time (bottom) on the MC sampling size. The black dashed line in the bottom-left panel represents the linearity of slope 1. The right panels show the dependence of averaged variances in \bar{p}_1 and c_1 (top) and of the average computation time (bottom) on the batch size for the flipout estimator, all with an MC sampling size of 4096. The black dashed line in the bottom-right panel represents the inverse linearity of slope -1 . All results are based on the data presented in Fig. 2

B. Model Calibration and Reliability

It has been suggested that the confidence of the predictions from a neural network classifier may be justified directly via its predictive values. That is to compare its predictive values with the empirical frequencies of the input data [75–77]. If they match well, this neural network classifier is said to have been well-calibrated and thus possesses confidence in its reliability. To this end, we first followed the method in Ref. [75] to produce the reliability curve, and then computed the expected calibration error (ECE) as defined in Ref. [76], using our validation dataset generated in Sec. II C 3. Each of the 4096 samples in our validation dataset possesses 15 time windows, each with a predictive value \bar{p}_1 . To construct the reliability curve, all these 4096×15 time windows were sorted in their associated \bar{p}_1 and then divided into 10 bins of roughly equal size. Within each bin, the \bar{p}_1 's were averaged to become the horizontal coordinate in the left panel of Fig. 11, while the actual fraction of real events (the positives) formed the vertical coordinate. The 10 bins thus generated 10 points in the plot, linked to form the reliability curve (the red solid line). Ideally we would like this curve to be as close as possible to the perfect

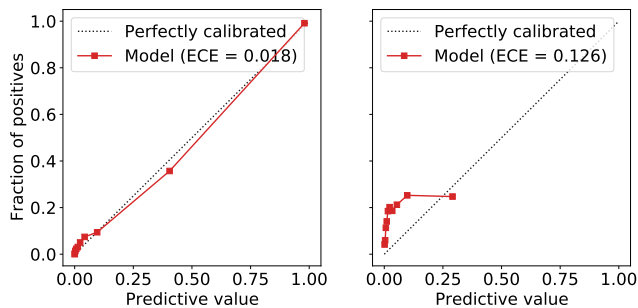


FIG. 11. The reliability curves of our model based on the validation dataset (left) and on only a subset with a low SNR of $\rho_{\text{opt}} = 2.5$ (right).

curve, which has a slope of one through the origin (the dotted line). It is clear that our model is fairly well-calibrated with a very small error of $\text{ECE} = 0.018$. We could thus conclude that the \bar{p}_1 generated by our model is a confident estimate for reality.

However, such confidence may break down in the following two cases. The first is when the input data does not follow the same distribution as the training dataset. The fact that our model, currently trained with only the BBH events, is insensitive to the BNS events is one example (see Sec. III B). This is why we introduced and utilized the confidence score c_k (see Eq. (7)) in our work. The confidence score would be low whenever the input data do not comply with the underlying distribution of the training data. This out-of-distribution problem can be minimized by training our model with datasets of all possible kinds that we may encounter during the observation.

The second case for the confidence breakdown is when the signal-to-noise ratio is not high enough so that the model fails to detect all the features it is supposed to recognize. To demonstrate this point, we computed the reliability curve for a subset of our validation data with $\rho_{\text{opt}} = 2.5$. The right panel of Fig. 11 shows the result. The reliability curve (red solid) being well to the left of the perfect curve (dotted) with a significant error of $\text{ECE} = 0.126$ indicates under detection of real events (the positives). This is simply due to the obscuration of the GW signals by the noise. Such a problem can be readily improved by deepening our model training to gain higher sensitivity.

To sum up, we may train our model deeper to gain higher sensitivity and also feed it with more signal types to avoid the breakdown of confidence. Furthermore, as long as our model possesses high enough sensitivity through deep training, our uncertainty estimation based on the confidence score could serve as a powerful tool for picking up the out-of-distribution signals that we have never seen before.

C. Stride Size of Sliding Window

The architecture of our model combines the CNN model and the sliding-window searches. Here we illustrate the effect of the stride size of our sliding windows. In principle, while keeping the same window size, a smaller stride size will increase the time resolution in pinning down a GW event. Fig. 12 shows the flagging results of the LIGO Livingston GW170809 data using stride sizes of 0.25 (top) and 0.7 (bottom) second, to be compared with our previous result for using 0.5 second (the fourth panel in Fig. 6). All time windows have the same size of one second. It is evident that the 0.25-second result performs the best in locating the GW event.

The only drawback for a smaller stride size is that the computation time is inversely increasing with the stride size, so there is always a trade-off given the available computation power. Another issue concerning the stride size is that a stride size larger than half of the window size will cause an un-uniform coverage of the time domain in the flagging analysis, leading to possible misses for the GW events [29]. Therefore it is optimal to choose a stride size of half the window size in face of the always limited computation power. In the main work presented in this paper we have chosen a window size of one second with a stride size of 0.5 second. When analyzing the forthcoming new data in future, one can always use our model here to first efficiently identify a GW event, hopefully in nearly real time, and then focus on the identified data chunks with increased time resolution and deeper search or even further using the matched-filtering search to pinpoint the coalescence time.

D. Forecasting GW Events

It is always desirable to be able to detect the GW waves before a coalescence event so that we could conduct parallel targeted observations such as the electromagnetic observations to trace the full process including the inspiral, merger and ringdown phases. A similar desire in the trading market has actually led to using the RNN model to perform time-series forecasting in detecting the anomaly in time series [78] and in predicting the stock price [79]. However our techniques based on deep learning for detecting GW waves rely strongly on recognizing the features of the GW waveform around the coalescence time, where the SNR is much stronger. This in turn implies that our model could detect the GW signals likely only when a coalescence event has come into the scene, and then we trace back in time to identify the data sections that may have contained the GW waveform before the event.

We verify this here using the Livingston GW170608 data. The results are shown in Fig. 13, where the bottom panel contains only one extra second where the coalescence event sits in its middle. The top panel shows no sign of GW detection even though the event is about

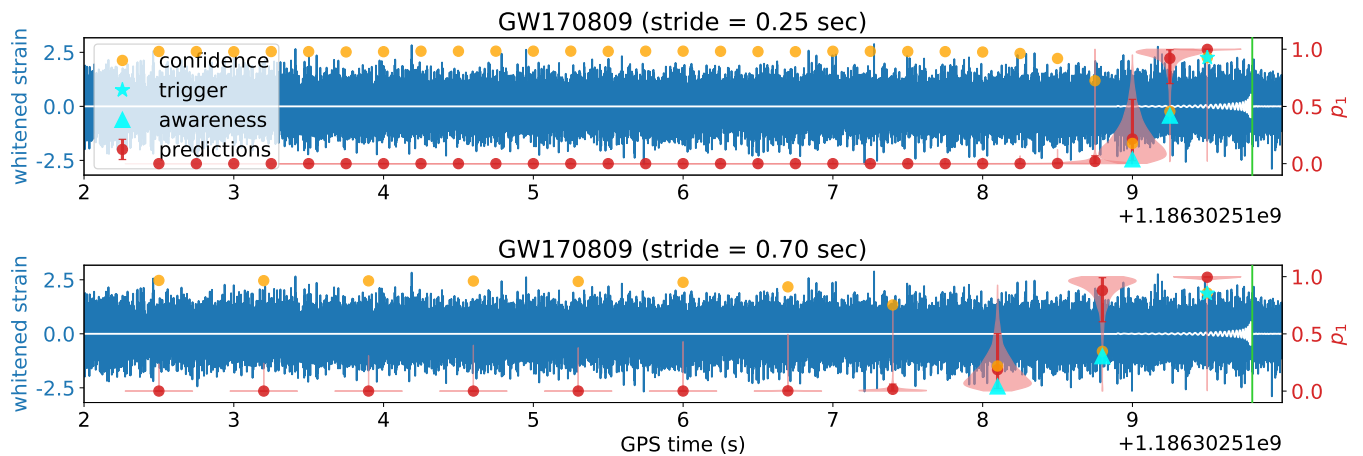


FIG. 12. The flagging results of the Livingston GW170809 data using sliding-window search with stride sizes of 0.25 second (top) and 0.7 second (bottom).

to enter our time domain of analysis, only half a second away. Once the event enters our time domain (bottom panel), our model immediately picks up all the time windows containing not only the event but also the waveform prior to the event. This is not surprising because for each forward pass our model uses the zero states as the initial hidden and cell states. To enable the capability for prior detections, we have to incorporate the hidden and cell states of the previous prediction into our model. This would require not only modifications in our model structure but also the construction of partly correlated samples in the training dataset. An extra complication is that the Bayesian Neural Networks would need to have all the previous hidden and cell states in the form of distributions. Considering these challenges we will leave the attempts for forecasting to future work.

V. CONCLUSION

We have proposed a new model to demonstrate the capability of Bayesian Neural Networks in detecting gravitational waves. One critical bonus for using the BNN is the ability for uncertainty estimation, which is particularly useful when facing the data that do not follow the distribution of the training dataset. Our uncertainty estimation is manifested by the newly defined confidence score c_1 , which in turn defines the ‘awareness state’ for collecting the cases where triggers cannot be accepted nor rejected with confidence. These cases can then be further investigated in the follow-up checks. In addition, our Bayesian CLDNN model integrates the CNN classifier with the sliding-window search scheme so that we could detect most of the time windows that contain the GW waveform in a coalescence event. However due to the limited computation power of this work, our current model does not outperform the sensitivity of the existing matched-filtering search but still successfully detect all the GW events that LIGO detected in the O2 observation. Nevertheless on a moderate GPU-equipped personal computer, it takes only about 20 seconds for detecting an event and labeling its waveform period whenever a coalescence event comes into the time domain of our analysis. This 20-second latency is expected to be dramatically improved by a GPU-optimized code with enhanced computation power and even shorter data chunks, making our model possible for nearly real-time detection. Such nearly real-time detection is unlikely to be possible for the matched-filtering search, which is always computationally expensive. In future we plan to further explore the discussed potential for a Bayesian CLDNN model in forecasting the GW coalescence events.

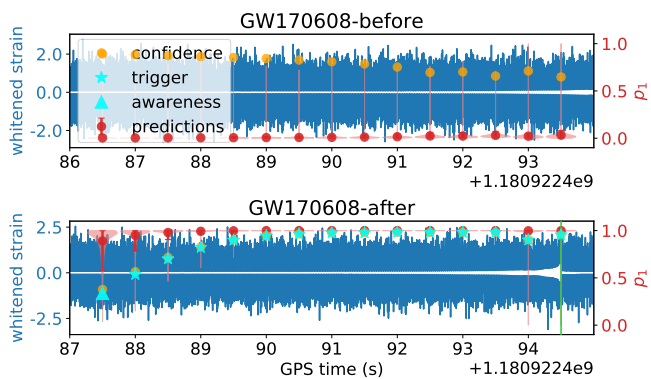


FIG. 13. The flagging results on the Livingston GW170608 data without the coalescence event (top) and with the event (bottom). The only difference between these two sub-datasets is the inclusion of the extra one second (on the right) in the bottom panel where the event sits in the middle of this second.

ACKNOWLEDGMENTS

We would like to thank Chun Hsiang Chang for useful discussions on deep learning and statistics. This research has used the data, software and/or web tools from the Gravitational Wave Open Science Center (<https://www.gw-openscience.org>), a service of LIGO

Laboratory, the LIGO Scientific Collaboration and the Virgo Collaboration. LIGO is funded by the U.S. National Science Foundation. Virgo is funded by the French Centre National de Recherche Scientifique (CNRS), the Italian Istituto Nazionale della Fisica Nucleare (INFN) and the Dutch Nikhef, with contributions by Polish and Hungarian institutes. We acknowledge the support from Ministry of Science and Technology, Taiwan.

-
- [1] B. P. Abbott *et al.* (LIGO Scientific Collaboration and Virgo Collaboration), Observation of gravitational waves from a binary black hole merger, *Phys. Rev. Lett.* **116**, 061102 (2016).
- [2] B. P. Abbott *et al.*, Advanced LIGO, *Classical and Quantum Gravity* **32**, 074001 (2015).
- [3] F. Acernese *et al.*, Advanced virgo: a second-generation interferometric gravitational wave detector, *Classical and Quantum Gravity* **32**, 024001 (2014).
- [4] B. P. Abbott *et al.* (LIGO Scientific Collaboration and Virgo Collaboration), Gw151226: Observation of gravitational waves from a 22-solar-mass binary black hole coalescence, *Phys. Rev. Lett.* **116**, 241103 (2016).
- [5] B. P. Abbott *et al.* (LIGO Scientific Collaboration and Virgo Collaboration), Binary black hole mergers in the first advanced ligo observing run, *Phys. Rev. X* **6**, 041015 (2016).
- [6] B. P. Abbott *et al.* (LIGO Scientific and Virgo Collaboration), Gw170104: Observation of a 50-solar-mass binary black hole coalescence at redshift 0.2, *Phys. Rev. Lett.* **118**, 221101 (2017).
- [7] B. P. Abbott *et al.*, GW170608: Observation of a 19 solar-mass binary black hole coalescence, *The Astrophysical Journal* **851**, L35 (2017).
- [8] B. P. Abbott *et al.* (LIGO Scientific Collaboration and Virgo Collaboration), Gw170814: A three-detector observation of gravitational waves from a binary black hole coalescence, *Phys. Rev. Lett.* **119**, 141101 (2017).
- [9] B. P. Abbott *et al.* (LIGO Scientific, Virgo), GWTC-1: A Gravitational-Wave Transient Catalog of Compact Binary Mergers Observed by LIGO and Virgo during the First and Second Observing Runs, *Phys. Rev.* **X9**, 031040 (2019), [arXiv:1811.12907 \[astro-ph.HE\]](https://arxiv.org/abs/1811.12907).
- [10] B. P. Abbott *et al.* (LIGO Scientific, Virgo), GW170817: Observation of Gravitational Waves from a Binary Neutron Star Inspiral, *Phys. Rev. Lett.* **119**, 161101 (2017), [arXiv:1710.05832 \[gr-qc\]](https://arxiv.org/abs/1710.05832).
- [11] A. Goldstein *et al.*, An ordinary short gamma-ray burst with extraordinary implications:fermi-GBM detection of GRB 170817a, *The Astrophysical Journal* **848**, L14 (2017).
- [12] V. Savchenko *et al.*, INTEGRALDetection of the first prompt gamma-ray signal coincident with the gravitational-wave event GW170817, *The Astrophysical Journal* **848**, L15 (2017).
- [13] B. P. Abbott *et al.*, Gravitational waves and gamma-rays from a binary neutron star merger: GW170817 and GRB 170817a, *The Astrophysical Journal* **848**, L13 (2017).
- [14] M. Soares-Santos *et al.* (DES, LIGO Scientific, Virgo), First Measurement of the Hubble Constant from a Dark Standard Siren using the Dark Energy Survey Galaxies and the LIGO/Virgo BinaryBlack-hole Merger GW170814, *Astrophys. J.* **876**, L7 (2019), [arXiv:1901.01540 \[astro-ph.CO\]](https://arxiv.org/abs/1901.01540).
- [15] B. P. Abbott *et al.* (LIGO Scientific, Virgo), Constraints on cosmic strings using data from the first Advanced LIGO observing run, *Phys. Rev.* **D97**, 102002 (2018), [arXiv:1712.01168 \[gr-qc\]](https://arxiv.org/abs/1712.01168).
- [16] T. Akutsu *et al.* (KAGRA), KAGRA: 2.5 Generation Interferometric Gravitational Wave Detector, *Nat. Astron.* **3**, 35 (2019), [arXiv:1811.08079 \[gr-qc\]](https://arxiv.org/abs/1811.08079).
- [17] B. Iyer, T. Souradeep, C. Unnikrishnan, S. Dhurandhar, S. Raja, and A. Sengupta, *Ligo-india, proposal of the consortium for indian initiative in gravitational-wave observations (indigo)* (2011), IIGO-M1100296-v2.
- [18] B. P. Abbott *et al.*, Prospects for observing and localizing gravitational-wave transients with advanced ligo, advanced virgo and kagra, *Living Reviews in Relativity* **21**, 3 (2018).
- [19] B. J. Owen and B. S. Sathyaprakash, Matched filtering of gravitational waves from inspiraling compact binaries: Computational cost and template placement, *Phys. Rev.* **D60**, 022002 (1999), [arXiv:gr-qc/9808076 \[gr-qc\]](https://arxiv.org/abs/gr-qc/9808076).
- [20] A. Nitz, I. Harry, D. Brown, C. M. Biwer, J. Willis, T. D. Canton, C. Capano, L. Pekowsky, T. Dent, A. R. Williamson, S. De, G. Davies, M. Cabero, D. Macleod, B. Machenschalk, S. Reyes, P. Kumar, T. Massinger, F. Pannarale, dfinstad, M. Tpai, S. Fairhurst, S. Khan, L. Singer, A. Nielsen, shasvath, S. Kumar, idorrington92, H. Gabbard, and B. U. V. Gadre, *gwastro/pycbc: Pycbc release v1.15.2* (2019).
- [21] S. A. Usman, A. H. Nitz, I. W. Harry, C. M. Biwer, D. A. Brown, M. Cabero, C. D. Capano, T. D. Canton, T. Dent, S. Fairhurst, M. S. Kehl, D. Keppel, B. Krishnan, A. Lenon, A. Lundgren, A. B. Nielsen, L. P. Pekowsky, H. P. Pfeiffer, P. R. Saulson, M. West, and J. L. Willis, The PyCBC search for gravitational waves from compact binary coalescence, *Classical and Quantum Gravity* **33**, 215004 (2016).
- [22] S. Sachdev *et al.*, The GstLAL Search Analysis Methods for Compact Binary Mergers in Advanced LIGO's Second and Advanced Virgo's First Observing Runs, (2019), [arXiv:1901.08580 \[gr-qc\]](https://arxiv.org/abs/1901.08580).
- [23] C. Messick, K. Blackburn, P. Brady, P. Brockill, K. Cannon, R. Cariou, S. Caudill, S. J. Chamberlin, J. D. E. Creighton, R. Everett, C. Hanna, D. Keppel, R. N. Lang, T. G. F. Li, D. Meacher, A. Nielsen, C. Pankow, S. Privitera, H. Qi, S. Sachdev, L. Sadeghian, L. Singer, E. G. Thomas, L. Wade, M. Wade, A. Weinstein, and K. Wiesner, Analysis framework for the prompt discovery of compact binary mergers in gravitational-wave data, *Phys. Rev. D* **95**, 042001 (2017).

- [24] J. Hertz, A. Krogh, and R. G. Palmer, *Introduction to the Theory of Neural Computation* (Addison-Wesley Longman Publishing Co., Inc., Boston, MA, USA, 1991).
- [25] Y. LeCun, B. Boser, J. S. Denker, D. Henderson, R. E. Howard, W. Hubbard, and L. D. Jackel, Backpropagation applied to handwritten zip code recognition, *Neural Computation* **1**, 541 (1989).
- [26] H. Sak, A. Senior, and F. Beaufays, Long short-term memory recurrent neural network architectures for large scale acoustic modeling, Proceedings of the Annual Conference of the International Speech Communication Association, INTERSPEECH , 338 (2014).
- [27] D. George and E. A. Huerta, Deep Neural Networks to Enable Real-time Multimessenger Astrophysics, *Phys. Rev.* **D97**, 044039 (2018), [arXiv:1701.00008 \[astro-ph.IM\]](#).
- [28] D. George and E. A. Huerta, Deep Learning for Real-time Gravitational Wave Detection and Parameter Estimation: Results with Advanced LIGO Data, *Phys. Lett.* **B778**, 64 (2018), [arXiv:1711.03121 \[gr-qc\]](#).
- [29] T. D. Gebhard, N. Kilbertus, I. Harry, and B. Schlkopf, Convolutional neural networks: a magic bullet for gravitational-wave detection? (2019) [arXiv:1904.08693 \[astro-ph.IM\]](#).
- [30] H. Gabbard, M. Williams, F. Hayes, and C. Messenger, Matching matched filtering with deep networks for gravitational-wave astronomy, *Phys. Rev. Lett.* **120**, 141103 (2018), [arXiv:1712.06041 \[astro-ph.IM\]](#).
- [31] X. Fan, J. Li, X. Li, Y. Zhong, and J. Cao, Applying deep neural networks to the detection and space parameter estimation of compact binary coalescence with a network of gravitational wave detectors, *Science China Physics, Mechanics, and Astronomy* **62**, 969512 (2019), [arXiv:1811.01380 \[astro-ph.IM\]](#).
- [32] P. G. Krastev, Real-Time Detection of Gravitational Waves from Binary Neutron Stars using Artificial Neural Networks, (2019), [arXiv:1908.03151 \[astro-ph.IM\]](#).
- [33] B. Lin, X. Li, and W. Yu, Binary Neutron Stars Gravitational Wave Detection Based on Wavelet Packet Analysis And Convolutional Neural Networks, arXiv e-prints (2019), [arXiv:1910.10525 \[astro-ph.IM\]](#).
- [34] M. Zevin *et al.*, Gravity Spy: Integrating Advanced LIGO Detector Characterization, Machine Learning, and Citizen Science, *Class. Quant. Grav.* **34**, 064003 (2017), [arXiv:1611.04596 \[gr-qc\]](#).
- [35] D. George, H. Shen, and E. A. Huerta, Deep Transfer Learning: A new deep learning glitch classification method for advanced LIGO, (2017), [arXiv:1706.07446 \[gr-qc\]](#).
- [36] M. Llorens-Monteagudo, A. Torres-Forn, J. A. Font, and A. Marquina, Classification of gravitational-wave glitches via dictionary learning, *Class. Quant. Grav.* **36**, 075005 (2019), [arXiv:1811.03867 \[astro-ph.IM\]](#).
- [37] S. B. Coughlin *et al.*, Classifying the unknown: discovering novel gravitational-wave detector glitches using similarity learning, *Phys. Rev.* **D99**, 082002 (2019), [arXiv:1903.04058 \[astro-ph.IM\]](#).
- [38] H. Shen, D. George, E. A. Huerta, and Z. Zhao, Denoising Gravitational Waves with Enhanced Deep Recurrent Denoising Auto-Encoders [10.1109/ICASSP.2019.8683061](#) (2019), [arXiv:1903.03105 \[astro-ph.CO\]](#).
- [39] W. Wei and E. A. Huerta, Gravitational Wave Denoising of Binary Black Hole Mergers with Deep Learning, *Phys. Lett.* **B800**, 135081 (2020), [arXiv:1901.00869 \[gr-qc\]](#).
- [40] H. Shen, D. George, E. A. Huerta, and Z. Zhao, Denoising Gravitational Waves using Deep Learning with Recurrent Denoising Autoencoders, (2017), [arXiv:1711.09919 \[gr-qc\]](#).
- [41] A. Nguyen, J. Yosinski, and J. Clune, Deep neural networks are easily fooled: High confidence predictions for unrecognizable images, *Computer Vision and Pattern Recognition (CVPR), 2015 IEEE Conference on*, (2015).
- [42] D. J. C. MacKay, A practical bayesian framework for backpropagation networks, *Neural Comput.* **4**, 448 (1992).
- [43] G. E. Hinton and R. M. Neal, Bayesian learning for neural networks (1995).
- [44] Y. Gal and Z. Ghahramani, Dropout as a Bayesian Approximation: Representing Model Uncertainty in Deep Learning, arXiv e-prints (2015), [arXiv:1506.02142 \[stat.ML\]](#).
- [45] A. Graves, Practical variational inference for neural networks, in *Proceedings of the 24th International Conference on Neural Information Processing Systems*, NIPS'11 (Curran Associates Inc., USA, 2011) pp. 2348–2356.
- [46] C. Blundell, J. Cornebise, K. Kavukcuoglu, and D. Wierstra, Weight Uncertainty in Neural Networks, arXiv e-prints (2015), [arXiv:1505.05424 \[stat.ML\]](#).
- [47] Y. Wen, P. Vicol, J. Ba, D. Tran, and R. Grosse, Flipout: Efficient Pseudo-Independent Weight Perturbations on Mini-Batches, arXiv e-prints (2018), [arXiv:1803.04386 \[cs.LG\]](#).
- [48] D. P. Kingma and M. Welling, Auto-Encoding Variational Bayes, arXiv e-prints (2013), [arXiv:1312.6114 \[stat.ML\]](#).
- [49] D. P. Kingma, T. Salimans, and M. Welling, Variational Dropout and the Local Reparameterization Trick, arXiv e-prints (2015), [arXiv:1506.02557 \[stat.ML\]](#).
- [50] M. Fortunato, C. Blundell, and O. Vinyals, Bayesian Recurrent Neural Networks, arXiv e-prints (2017), [arXiv:1704.02798 \[cs.LG\]](#).
- [51] T. N. Sainath, O. Vinyals, A. Senior, and H. Sak, Convolutional, long short-term memory, fully connected deep neural networks, in *2015 IEEE International Conference on Acoustics, Speech and Signal Processing (ICASSP)* (2015) pp. 4580–4584.
- [52] M. I. Jordan, Z. Ghahramani, T. S. Jaakkola, and L. K. Saul, An introduction to variational methods for graphical models, *Machine Learning* **37**, 183 (1999).
- [53] S. Kullback and R. A. Leibler, On information and sufficiency, *Ann. Math. Statist.* **22**, 79 (1951).
- [54] S. Kullback, *Information theory and statistics* (Courier Corporation, 1997).
- [55] A. Kendall and Y. Gal, What uncertainties do we need in bayesian deep learning for computer vision?, in *Advances in Neural Information Processing Systems 30*, edited by I. Guyon, U. V. Luxburg, S. Bengio, H. Wallach, R. Fergus, S. Vishwanathan, and R. Garnett (Curran Associates, Inc., 2017) pp. 5574–5584.
- [56] Y. Kwon, J.-H. Won, B. J. Kim, and M. C. Paik, Uncertainty quantification using bayesian neural networks in classification: Application to ischemic stroke lesion segmentation (2018).
- [57] G. Deodato, C. Ball, and X. Zhang, Bayesian neural networks for cellular image classification and uncertainty analysis, *bioRxiv* [10.1101/824862](#) (2019).
- [58] T. Gebhard, N. Kilbertus, G. Parascandolo, I. Harry, and B. Schölkopf, Convwave: Searching for gravitational

- waves with fully convolutional neural nets, in *Workshop on Deep Learning for Physical Sciences (DLPS) at the 31st Conference on Neural Information Processing Systems* (2017).
- [59] A. van den Oord, S. Dieleman, H. Zen, K. Simonyan, O. Vinyals, A. Graves, N. Kalchbrenner, A. Senior, and K. Kavukcuoglu, WaveNet: A Generative Model for Raw Audio, arXiv e-prints, arXiv:1609.03499 (2016), arXiv:1609.03499 [cs.SD].
- [60] M. Riesenhuber and T. Poggio, Hierarchical models of object recognition in cortex, *Nature Neuroscience* **2**, 1019 (1999).
- [61] S. Ioffe and C. Szegedy, Batch normalization: Accelerating deep network training by reducing internal covariate shift, *CoRR abs/1502.03167* (2015), arXiv:1502.03167.
- [62] V. Nair and G. E. Hinton, Rectified linear units improve restricted boltzmann machines, in *ICML* (2010).
- [63] M. Vallisneri, J. Kanner, R. Williams, A. Weinstein, and B. Stephens, The LIGO Open Science Center, *Proceedings, 10th International LISA Symposium: Gainesville, Florida, USA, May 18-23, 2014*, *J. Phys. Conf. Ser.* **610**, 012021 (2015), arXiv:1410.4839 [gr-qc].
- [64] LIGO Scientific Collaboration, *LIGO Algorithm Library - LALSuite*, free software (GPL) (2018).
- [65] A. Boh *et al.*, Improved effective-one-body model of spinning, nonprecessing binary black holes for the era of gravitational-wave astrophysics with advanced detectors, *Phys. Rev.* **D95**, 044028 (2017), arXiv:1611.03703 [gr-qc].
- [66] B. S. Sathyaprakash and B. F. Schutz, Physics, Astrophysics and Cosmology with Gravitational Waves, *Living Rev. Rel.* **12**, 2 (2009), arXiv:0903.0338 [gr-qc].
- [67] M. Abadi, A. Agarwal, P. Barham, E. Brevdo, Z. Chen, C. Citro, G. S. Corrado, A. Davis, J. Dean, M. Devin, S. Ghemawat, I. Goodfellow, A. Harp, G. Irving, M. Isard, Y. Jia, R. Jozefowicz, L. Kaiser, M. Kudlur, J. Levenberg, D. Mané, R. Monga, S. Moore, D. Murray, C. Olah, M. Schuster, J. Shlens, B. Steiner, I. Sutskever, K. Talwar, P. Tucker, V. Vanhoucke, V. Vasudevan, F. Viégas, O. Vinyals, P. Warden, M. Wattenberg, M. Wicke, Y. Yu, and X. Zheng, *TensorFlow: Large-scale machine learning on heterogeneous systems* (2015), software available from tensorflow.org.
- [68] J. V. Dillon, I. Langmore, D. Tran, E. Brevdo, S. Vasudevan, D. Moore, B. Patton, A. Alemi, M. Hoffman, and R. A. Saurous, TensorFlow Distributions, arXiv e-prints (2017), arXiv:1711.10604 [cs.LG].
- [69] D. P. Kingma and J. Ba, Adam: A Method for Stochastic Optimization, arXiv e-prints (2014), arXiv:1412.6980 [cs.LG].
- [70] B. P. Abbott *et al.*, Low-latency gravitational-wave alerts for multimessenger astronomy during the second advanced LIGO and virgo observing run, *The Astrophysical Journal* **875**, 161 (2019).
- [71] C. Pankow *et al.*, Mitigation of the instrumental noise transient in gravitational-wave data surrounding GW170817, *Phys. Rev.* **D98**, 084016 (2018), arXiv:1808.03619 [gr-qc].
- [72] M. Boyle, D. A. Brown, L. E. Kidder, A. H. Mroue, H. P. Pfeiffer, M. A. Scheel, G. B. Cook, and S. A. Teukolsky, High-accuracy comparison of numerical relativity simulations with post-Newtonian expansions, *Phys. Rev.* **D76**, 124038 (2007), arXiv:0710.0158 [gr-qc].
- [73] C. Szegedy, W. Zaremba, I. Sutskever, J. Bruna, D. Erhan, I. Goodfellow, and R. Fergus, Intriguing properties of neural networks, arXiv e-prints (2013), arXiv:1312.6199 [cs.CV].
- [74] N. Akhtar and A. Mian, Threat of adversarial attacks on deep learning in computer vision: A survey, *IEEE Access* **6**, 14410 (2018).
- [75] A. Niculescu-Mizil and R. Caruana, Predicting good probabilities with supervised learning, in *ICML* (2005).
- [76] M. Pakdaman Naeini, G. Cooper, and M. Hauskrecht, Obtaining well calibrated probabilities using bayesian binning, *Proceedings of the ... AAAI Conference on Artificial Intelligence. AAAI Conference on Artificial Intelligence* **2015**, 2901 (2015).
- [77] C. Guo, G. Pleiss, Y. Sun, and K. Q. Weinberger, On calibration of modern neural networks, *CoRR abs/1706.04599* (2017), arXiv:1706.04599.
- [78] P. Malhotra, L. Vig, G. Shroff, and P. Agarwal, Long short term memory networks for anomaly detection in time series (2015).
- [79] A. Elliot and C. H. Hsu, Time Series Prediction : Predicting Stock Price, arXiv e-prints (2017), arXiv:1710.05715 [stat.ML].